



HAL
open science

Investigation of electron trapping in AlGa_N/Ga_N HEMT with Fe-doped buffer through DCT characterization and TCAD device simulations

Mohamed Bouslama, P. Vigneshwara Raja, Florent Gaillard, Raphaël Sommet, Jean-Christophe Nallatamby

► To cite this version:

Mohamed Bouslama, P. Vigneshwara Raja, Florent Gaillard, Raphaël Sommet, Jean-Christophe Nallatamby. Investigation of electron trapping in AlGa_N/Ga_N HEMT with Fe-doped buffer through DCT characterization and TCAD device simulations. *AIP Advances*, 2021, 11 (12), pp.125316. 10.1063/5.0064493 . hal-03482467

HAL Id: hal-03482467

<https://hal.science/hal-03482467>

Submitted on 11 Oct 2022

HAL is a multi-disciplinary open access archive for the deposit and dissemination of scientific research documents, whether they are published or not. The documents may come from teaching and research institutions in France or abroad, or from public or private research centers.

L'archive ouverte pluridisciplinaire **HAL**, est destinée au dépôt et à la diffusion de documents scientifiques de niveau recherche, publiés ou non, émanant des établissements d'enseignement et de recherche français ou étrangers, des laboratoires publics ou privés.

Investigation of electron trapping in AlGaIn/GaN HEMT with Fe-doped buffer through DCT characterization and TCAD device simulations

Cite as: AIP Advances 11, 125316 (2021); <https://doi.org/10.1063/5.0064493>

Submitted: 13 September 2021 • Accepted: 25 November 2021 • Published Online: 15 December 2021

 Mohamed Bouslama, P. Vigneshwara Raja, Florent Gaillard, et al.



View Online



Export Citation



CrossMark

ARTICLES YOU MAY BE INTERESTED IN

[GaN-based power devices: Physics, reliability, and perspectives](#)

Journal of Applied Physics **130**, 181101 (2021); <https://doi.org/10.1063/5.0061354>

[Emerging GaN technologies for power, RF, digital, and quantum computing applications: Recent advances and prospects](#)

Journal of Applied Physics **130**, 160902 (2021); <https://doi.org/10.1063/5.0061555>

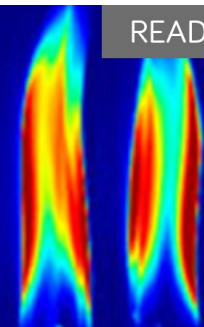
[Two-dimensional electron gases induced by spontaneous and piezoelectric polarization charges in N- and Ga-face AlGaIn/GaN heterostructures](#)

Journal of Applied Physics **85**, 3222 (1999); <https://doi.org/10.1063/1.369664>

AIP Advances

Fluids and Plasmas Collection

READ NOW



Investigation of electron trapping in AlGaIn/GaN HEMT with Fe-doped buffer through DCT characterization and TCAD device simulations

Cite as: AIP Advances 11, 125316 (2021); doi: 10.1063/5.0064493
Submitted: 13 September 2021 • Accepted: 25 November 2021 •
Published Online: 15 December 2021



View Online



Export Citation



CrossMark

Mohamed Bouslama,  P. Vigneshwara Raja, Florent Gaillard, Raphael Sommet,
and Jean-Christophe Nallatamby^{a)} 

AFFILIATIONS

XLIM Laboratory, CNRS, UMR 7252, University of Limoges, F-19100 Brive, France

^{a)} Author to whom correspondence should be addressed: jean-christophe.nallatamby@unilim.fr

ABSTRACT

The electron trapping in AlGaIn/GaN high-electron mobility transistors (HEMTs) with iron (Fe)-doped buffer is investigated through Drain Current Transient (DCT) measurements and TCAD physics-based 2D device simulations. The DCT characterization reveals two prominent deep-level electron traps E1 (~0.5 eV) and E2 (~0.6 eV) in the AlGaIn/GaN HEMT. The measured DCT spectrum is analyzed at different trap-filling pulse durations (10 μ s–100 ms) to obtain the information of trapping kinetics. As the first step in the simulation, the TCAD physical model parameters are calibrated by matching the simulated DC characteristics with the experimental data. It is shown that the TCAD model incorporating the acceptor-type trap at $E_C - 0.5$ eV in the GaN buffer quantitatively reproduces the measured DCT spectra over the temperature range of 25–100 °C. To explore the buffer trapping effects, the simulated DCT is inspected by varying the activation energy, capture cross section, and concentration of the buffer trap.

© 2021 Author(s). All article content, except where otherwise noted, is licensed under a Creative Commons Attribution (CC BY) license (<http://creativecommons.org/licenses/by/4.0/>). <https://doi.org/10.1063/5.0064493>

I. INTRODUCTION

The GaN buffer layer is intentionally doped with compensational impurity such as iron (Fe) for reducing buffer leakage and punch-through currents, enhancing carrier confinement in the 2DEG and increasing the breakdown voltage of AlGaIn/GaN high-electron mobility transistor (HEMT) devices.^{1–5} The Fe-doping induced acceptor-like traps electrically compensate the residual background donor impurities in the buffer region, thereby resulting in a highly resistive GaN buffer layer.^{2,5} Nevertheless, electron trapping in the buffer promotes current collapse/dispersion, increased ON-resistance (R_{ON}) and dynamic shift in threshold voltage, and restricted microwave output power and efficiency, hindering the dynamic operation of the HEMT.^{1–4} Thus, buffer trapping is the major obstacle in the AlGaIn/GaN HEMT technology for its successive integration in next generation microwave and high-power systems. Hence, defect characterization and simulation studies are essential to acquire the information of deep-level traps in the device and to control Fe-doping incorporation in the buffer during the epitaxial layer growth.

Drain Current Transient (DCT) spectroscopy is a powerful time domain technique to characterize deep-level traps in AlGaIn/GaN HEMTs.^{4,6–13} The Low-Frequency (LF) output admittance (Y_{22})^{10,12–17} and drain noise^{18–20} characteristics have also been used to identify traps in HEMTs in the frequency domain. In our earlier works, buffer trapping influenced the Y_{22} parameters,^{13,15–17} and the drain noise¹⁹ properties of the AlGaIn/GaN HEMT were studied through the effective calibration of simulation results with the measured data. There are extensive reports in the literature on TCAD simulation analysis for drain current transient properties of the AlGaIn/GaN HEMT.^{6,21–31} Tirado *et al.*²³ analyzed trapping effects on the drain-lag and gate-lag transient responses of AlGaIn/GaN HEMTs and obtained good agreement between the simulated and experimental drain current transient characteristics at room temperature. Chini *et al.*³¹ identified from the TCAD simulations that the negative peak in the DCT derivative spectra (i.e., decreasing current step in the DCT) is produced due to the hole emission from the acceptor-like trap at $E_V + 0.9$ eV located in the carbon-doped GaN buffer layer. However, in most of the articles, simulated DCT

characteristics were compared with the measured spectra only under room temperature conditions. In this work, the DCT experiments are conducted to characterize the deep-level traps in the AlGaIn/GaN HEMT with Fe-doped buffer. After that, TCAD simulations are performed to investigate the buffer trapping effects on static I - V and DCT characteristics of the HEMT and also to identify the physical location of the deep-level traps. Particularly, the simulated DCT spectra are validated with the experimental data over the temperature range of 25–100 °C. Thus, the effective interpretation of measured DCT characteristics with the TCAD simulations is demonstrated in this work. Moreover, the simulated DCT is inspected as a function of buffer trap activation energy, capture cross section, and acceptor concentration to understand the buffer trapping impact on the DCT properties of the AlGaIn/GaN HEMT.

II. EXPERIMENT

The investigated HEMT device consists of a GaN/AlGaIn/GaN heterostructure grown on a silicon carbide (SiC) substrate. The epitaxial heterostructure layer contains an Fe-doped GaN buffer layer, undoped GaN channel layer, Al_{0.25}Ga_{0.75}N barrier layer, and thin GaN cap layer. The transistor features a T-gate design with 0.15 μm length and a gate width size of 8 × 50 μm². The AlGaIn/GaN HEMT device structure also has a source terminated field plate configuration and silicon nitride (SiN) surface passivation. Further details of the HEMT cannot be disclosed due to intellectual property rights.

A. DCT characterization

At first, static I_{DS} - V_{DS} and I_{DS} - V_{GS} properties of the HEMT were measured at room temperature by using the AMCAD AM 3200 pulsed I - V system. The drain current (I_{DS}) transient measurements were conducted by using 2 pulse generators (Agilent HP 81110A and HP8114A) and two DPOs (Tektronix DP07054) to monitor the drain current. The DCT characterization was carried out in two phases, and each transient spectrum was measured under isothermal conditions (in a stabilized temperature). In the initial phase, the drain voltage (V_{DS}) was increased from 10 to 20 V and retained for a sufficient amount of time to populate (fill) the traps in the device. In the second phase (after the trap-filling pulse t_f), V_{DS} was instantly reduced to 10 V, and the I_{DS} transient recovery spectrum was recorded with respect to time from 1 μs to 1 s (six decades of the time scale). The gate voltage (V_{GS}) was maintained at a particular bias in order to get $I_{DS} = \sim 50$ mA/mm during the DCT experiments. To compute the trap parameters from the Arrhenius relation, the DCT spectra were acquired for five different chuck temperatures from 25 to 125 °C. Moreover, the DCT characterization was performed by varying the duration of the trap-filling pulse ($t_f = 10$ μs, 100 μs, 1 ms, and 100 ms) to acquire the information of trapping kinetics.

III. SIMULATION DETAILS

The 2D device simulations are carried out in the commercial Sentaurus TCAD³² software from Synopsis Inc. The AlGaIn/GaN HEMT structure considered in the simulation is shown in Fig. 1. The Schottky contact is used for the gate metal with a work function of 4.7 eV, while the Ohmic contact is utilized for the source and drain electrodes. A fixed sheet charge having equal density

($\sigma_{pol} = \pm 1.23 \times 10^{13}$ cm⁻²) but opposite polarity is defined on either side of the AlGaIn barrier layer to emulate the polarization produced charge in the AlGaIn/GaN heterostructure.^{13,15,17,19,21,33–35} A fixed interface charge density ($\sigma_{interface}$) of -2×10^{12} cm⁻² is placed at the SiN/GaN interface to incorporate the charges existing in the SiN dielectric layer along with the polarization charge at this interface region.^{15,35,36} The physics-based models³² such as the drift-diffusion model for charge transport, temperature dependent carrier mobility due to bulk phonon scattering, the Canali carrier mobility model for high field saturation, no bandgap narrowing, Fermi statistics, thermionic emission at the heterojunction, Shockley–Read–Hall (SRH) recombination for trap-assisted carrier transition, and Auger recombination are considered in the simulation. The radiative recombination model is also activated to account for the band-to-band carrier transitions in the GaN and AlGaIn (direct bandgap) materials. The studied AlGaIn/GaN HEMT was fabricated on a high-thermal conductivity SiC substrate,^{13,17,33,37} and the adopted drain bias voltage range in the DC characterization is $V_{DS} \leq 10$ V, so the device self-heating effects are less pronounced in static I - V . Moreover, self-heating in the drain current transient response is found to be negligible.^{13,17,21,33} Hence, the thermal effects are not incorporated in the charge transport model.

The widely accepted surface donor model theory states that the surface donors are the major source of electrons for the 2DEG.^{38,39} If the AlGaIn barrier thickness exceeds the critical value ($d_{CR} \geq 3.5$ nm), the surface donor energy goes above (or reaches) the Fermi level; as a result, electrons are transferred from the surface donors (ensuing positively ionized donors σ_D^+ at the surface) to the AlGaIn/GaN interface and the subsequent formation of the 2DEG.^{38,39} The energy location of the surface donor has been empirically identified at $E_C - 1.65$ eV³⁹ (1.65 eV below the conduction band edge) in the Al_{0.34}Ga_{0.64}N/GaN heterostructure and at $E_C - 1.42$ eV³⁸ in the Al_{0.27}Ga_{0.73}N/GaN structure. Following the surface donor theory and experimental findings, in the simulation model, surface donor energy (E_{TD}) is located at $E_C - 1.4$ eV at the GaN/SiN ungated interface. The surface donor density (σ_D) is taken as 2×10^{13} cm⁻², along with the equal electron and hole capture cross-sections $\sigma_{nD} = \sigma_{pD} = 10^{-15}$ cm²; these values are more appropriate for validating the simulation results with the experimental data. Trap parameters deduced from the DCT experiments are included in the GaN buffer region as acceptor-like traps (discussed in Sec. IV). In a stationary state, the net carrier recombination rate (R_{net}) through a single trap level in the bandgap is implemented in the TCAD physical model as³²

$$R_{net} = \frac{N_0 v_{th}^n v_{th}^p \sigma_n \sigma_p (np - n_{ie}^2)}{v_{th}^n \sigma_n (n + n_1/g_n) + v_{th}^p \sigma_p (p + p_1/g_p)}, \quad (1)$$

where N_0 is the trap concentration, v_{th} is the carrier thermal velocity, σ is the capture cross section of the trap, and the n and p indices are associated with the electron and hole, respectively. Under the assumption of identical electron and hole capture cross sections ($\sigma_n = \sigma_p$) and unit degeneracy factors ($g_n = g_p = 1$), Eq. (1) can be further simplified in a form of well-known SRH approximation (R_{net}^{SRH}),³²

$$R_{net}^{SRH} = \frac{np - n_{ie}^2}{\tau_p(n + n_1) + \tau_n(p + p_1)}, \quad (2)$$

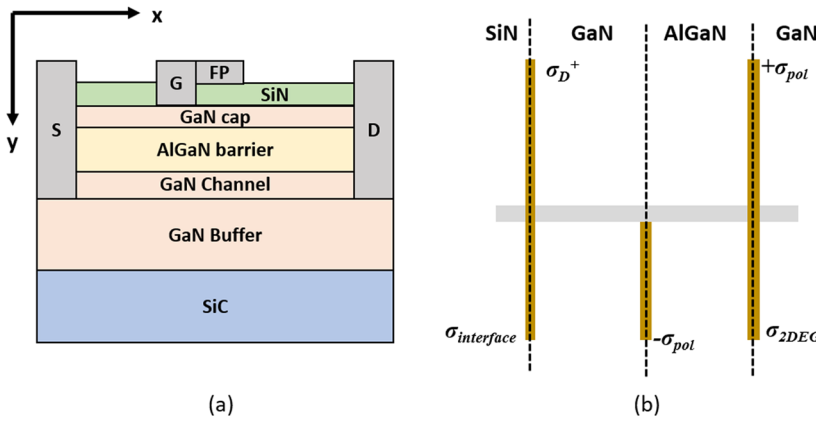


FIG. 1. (a) Schematic cross section of the GaN/AlGaN/GaN HEMT structure used in the simulation. (b) Polarization charges defined at each material interface in the physical device simulation.

where n is the electron concentration in the conduction band; p is the hole concentration in the valence band; n_{ie} is the effective intrinsic carrier density; τ_n and τ_p denote the effective electron and hole lifetimes, respectively, which are incorporated in the SRH recombination statistics as a doping-dependent, electric field-dependent, and temperature-dependent factor; and n_1 and p_1 represent the additional carrier concentrations corresponding to the trap energy,³²

$$n_1 = n_{ie} \exp(E_{trap}/kT), \quad p_1 = n_{ie} \exp(-E_{trap}/kT), \quad (3)$$

where E_{trap} indicates the energy difference between the trap level and intrinsic level, k is the Boltzmann constant, and T is the temperature. In the transient simulation, the rate of change in the electron occupancy (f^n) of a trap level (trap occupation dynamics) due to the electron capture and emission processes is given as³²

$$\frac{\partial f^n}{\partial t} = \sum_i r_{n,i} = \sum_i (1 - f^n) c_{n,i} - f^n e_{n,i}, \quad (4)$$

where $1 - f^n$ is the probability for a trap to be unoccupied by an electron, c_n is the electron capture rate for an unoccupied trap state, and e_n is the electron emission rate for an occupied trap state,³²

$$c_n = n \sigma_n v_{th}^n, \quad (5)$$

$$e_n = \frac{\sigma_n v_{th}^n N_C}{g} \exp\left(-\frac{E_C - E_T}{kT}\right), \quad (6)$$

where N_C is the effective density states in the conduction band (E_C) and E_T is the trap energy.

As the first step in the simulation, the static I - V characteristics of the HEMT are replicated to calibrate the TCAD physics-based model parameters. Afterward, the DCT simulations are performed in a mixed mode circuit configuration. A piecewise linear voltage source³² is selected for pulsing operation at the drain terminal based on the experimental V_{DS} switching conditions, whereas a DC voltage source is chosen for the gate terminal. After the trap-filling pulse, the I_{DS} transient sweep is started from the initial time of 1 μ s, and the sampling time of the transient is augmented according to the ramping step size and parameters until reaching the target time (1 s) of the sweep. Accordingly, the drain current transient recovery

spectrum of the HEMT is simulated over the six decades of the time scale (1 μ s–1 s). The simulated DCT spectra are obtained for different temperatures (25–100 °C) and also for the various trap-filling pulse durations ($t_f = 10 \mu$ s, 100 μ s, 1 ms, and 100 ms).

IV. RESULTS AND DISCUSSION

A. Measured DCT spectroscopy

Figure 2(a) shows the measured DCT spectra (filling time $t_f = 100$ ms) of the AlGaN/GaN HEMT with Fe-doped buffer for temperatures ranging from 25 to 125 °C. The gate voltage V_{GS} is kept constant in order to obtain a quiescent current of ~ 50 mA/mm, and the drain voltage V_{DS} is pulsed from 10 to 20 V and is maintained at 20 V for 100 ms; then, it is changed again to 10 V. The drain current transient response is measured just toward the end of the trap-filling drain pulse. These biasing conditions correspond to the deep class AB operation mode, which is widely used for designing RF power amplifiers. The increasing current trend in the DCT reveals that the I_{DS} transient recovery process may be due to the thermal emission of electrons from an active trap present in the device.^{7,9,13,31} To extract the emission time constant (τ_n) of the detrapping phenomena, the measured DCT data (I_{data}) are fitted by the sum of stretched exponential functions in a least mean square approach,^{4,6,7,9}

$$I_{fitting} = \sum_{i=1}^N A_0 + A_i \exp\left(\frac{-t}{\tau_{n,i}}\right)^{\beta_i}, \quad (7)$$

where N denotes the number of exponentials used for the DCT fitting ($I_{fitting}$), A_0 is the constant, A_i is the fitting parameter, and β_i is the stretching factor. The DCT fitting is effectively accomplished in such a way to minimize the $|I_{data} - I_{fitted}|^2$ error at the experimental data points.⁶ The dashed lines in Fig. 1(a) represent the fitted DCT spectra. Note that the unity stretching factor $\beta_i = 1$ is considered in all the fitted transients; thus, the carrier detrapping kinetics follow a pure (non-stretched) exponential behavior.^{4,7,30} On the other hand, the stretched exponential nature in the DCT can be represented by the condition $\beta_i \neq 1$.^{4,7} The derivative spectra [$\partial I_{DS}/\partial \log_{10}(t)$] of the fitted DCT data are plotted in Fig. 2(b). Two distinct positive peaks (labeled E1 and E2) are observed in the DCT derivative spectra. Among these peaks, E2 is visible in the DCT spectra only at higher temperatures (≥ 75 °C), suggesting that defect E2 is located deeper in

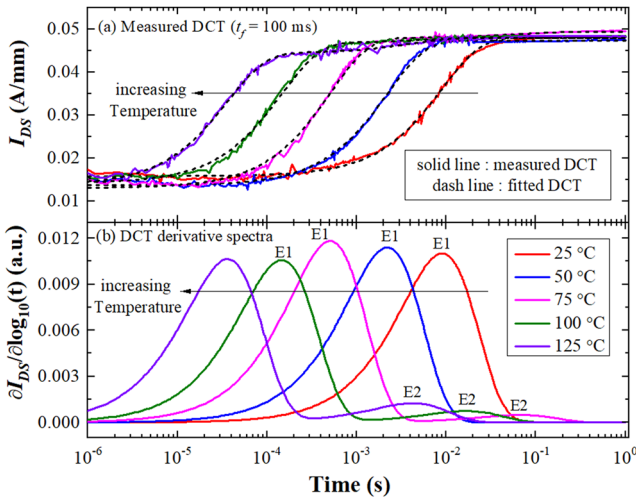


FIG. 2. (a) Measured DCT spectra (filling time $t_f = 100$ ms) for AlGaIn/GaN HEMT with Fe-doped buffer at different temperatures (25–125 °C); the dashed line represents the fitted DCT by the stretched multiexponential functions. (b) Derivative spectra $[\partial I_{DS}/\partial \log_{10}(t)]$ of fitted DCT data reveal two trap signatures E1 and E2.

the bandgap than E1. The peaks E1 and E2 are found to move toward lower time constants (τ_n) with increasing temperature, so the carrier emission rate is a thermally activated process, as per Eq. (6).

The information regarding the capture kinetics of the traps E1 and E2 can be obtained by analyzing the trap-filling time dependency on the DCT signal amplitude.^{2,4,7} Figures 3(a) and 3(b) depict the DCT derivative spectra of the HEMT acquired at the temperatures of 25 and 125 °C for different trap-filling times (t_f). There is

no considerable change in the $\partial I_{DS}/\partial \log_{10}(t)$ signal magnitude of trap E1 upon increasing the filling time from 10 μ s to 100 ms in the investigated temperature range (25–125 °C). Similarly, the E2 signal amplitude is almost unchanged at two different filling times $t_f = 1$ and 100 ms, as observed from Fig. 3(b). If the DCT signal has a logarithmic dependence on the trap-filling time, the respective trap level may be associated with the highly localized defect states (defect clustering along dislocations).^{2,7,40} In this case, the capture rate of the defects may be reduced due to the repulsive Coulomb barrier established by the already trapped electrons, so the defects clustered along dislocations may have variable capture cross section values.^{2,7,40} In this work, the DCT signal amplitude of E1 and E2 is unaffected by the duration of the filling pulse, specifying that the traps E1 and E2 are related to the point defects and are localized with identical capture cross sections.^{2,4,7}

The carrier emission time constant associated with the trap is extracted from the peak maximum position of the DCT derivative spectra. Accordingly, the emission time constant (τ_n) of E1 and E2 is noted at different temperatures, and the activation energy and capture cross section of the traps are calculated by using the rearranged emission rate equation (6),^{13–15}

$$\ln(\tau_n T^2) = \frac{\Delta E_a}{kT} - \ln\left(\frac{\sigma_n v_{th}^n N_C}{g T^2}\right). \quad (8)$$

Figure 4 shows the $\ln(\tau_n T^2)$ vs $1/kT$ plot for traps E1 and E2 obtained at various filling times $t_f = 10 \mu$ s to 100 ms. Typical Arrhenius-like properties (i.e., linear curve fitting) are observed in the emission time constants of E1 and E2; therefore, the trapping/detrapping dynamics associated with traps E1 and E2 are essentially governed by the conventional SRH recombination mechanism. The slope of the Arrhenius plot yields the activation energy of traps

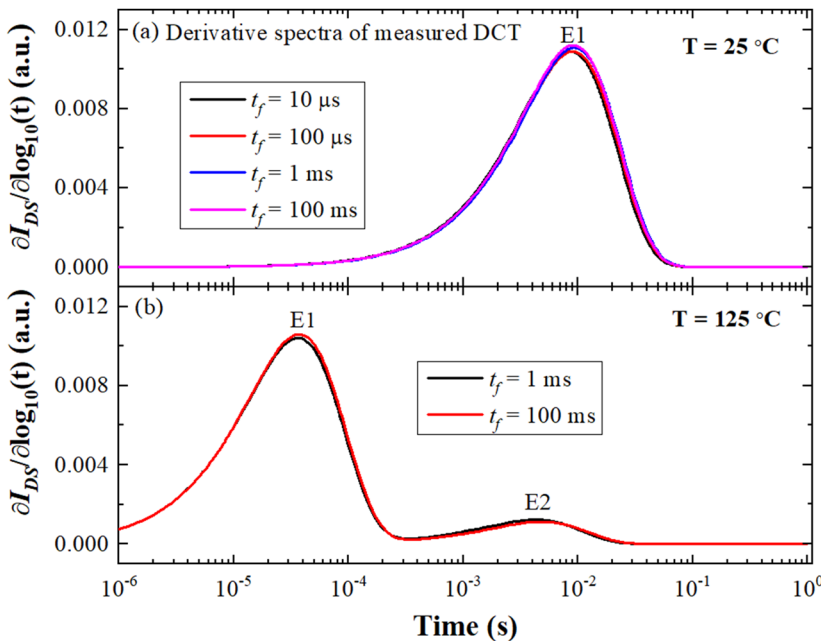


FIG. 3. (a) DCT derivative spectra acquired at the temperature $T = 25$ °C for various filling times ($t_f = 10 \mu$ s, 100 μ s, 1 ms, and 100 ms). (b) DCT derivative spectra at $T = 125$ °C for two different filling times ($t_f = 1$ and 100 ms).

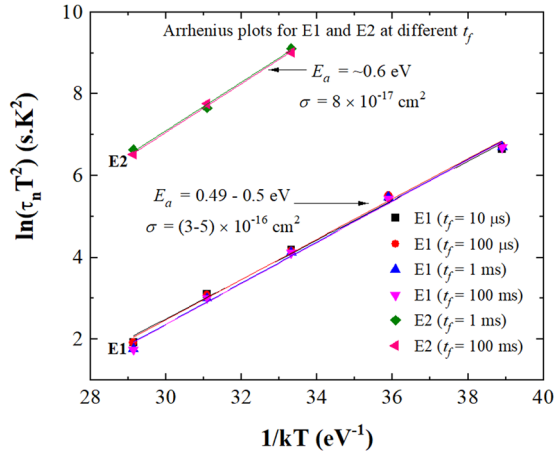


FIG. 4. Arrhenius plots for traps E1 and E2 obtained from the measured DCT at different trap-filling times (t_f).

E1 (0.49–0.5 eV) and E2 (~0.6 eV). From the intercept of the Arrhenius plots, the capture cross section (σ_{nA}) of defects E1 and E2 is calculated as $(3-5) \times 10^{-16}$ and $\sim 8 \times 10^{-17}$ cm², respectively. As trap E2 has a higher activation energy and lower capture cross section than E1, the DCT spectra show the evidence of E2 only at higher temperatures (≥ 75 °C) in the measured time range (1 μ s–1 s) by referring to the emission rate equation (6). Moreover, E2 is not detected in the DCT spectra attained for shorter filling times ($t_f < 1$ ms) possibly due to their low capture cross section of 8×10^{-17} cm², according to the capture rate equation (5). The increasing current steps in the DCT and the positive peaks in the derivative spectra suggest that E1 and E2 are electron traps positioned at the energy level $E_C - E_T$.^{7,9,13,31} As Fe-doping is employed in the GaN buffer layer, it is supposed that traps E1 and E2 may be related to the Fe-doping incorporation in the buffer. Nonetheless, at this point, the energy position (electron or hole trap), physical location (buffer or barrier), and type (acceptor or donor-like state) of the traps are still not verified from the experimental observations. Hence, the DCT simulations are performed to identify the energy position, spatial location, and nature of the traps.

B. Simulated DC characteristics

The main purpose of the static I - V simulation is to calibrate the TCAD physical model parameters. After many simulation iterations, it is found that the following material and physical parameters play a crucial role in deciding the DC characteristics of the HEMT:^{13,15,17,33,34,37} polarization charge (σ_{pol}) at the heterointerface, buffer trap energy (E_{TA}), concentration (N_{TA}), surface donor energy (E_{TD}), gate metal work function (Φ_G), electron mobility (μ_n), and saturation velocity (v_{sat}^n) in the GaN. Among these parameters, N_{TA} , μ_n , and v_{sat}^n values are varied for model calibration, while the other parameters are selected based on our experimental results and the literature data. The polarization charge at the AlGaIn/GaN heterointerface is computed based on the theoretical model by Ambacher *et al.*⁴¹ The total polarization charge (P_{pol}) in the device

structure comprises the strain induced piezoelectric polarization (P_{PE}) component and the spontaneous polarization (P_{SP}) component,^{41,42}

$$P_{pol} = (P_{PE} + P_{SP})_{AlGaIn} - P_{SPGaIn}, \quad (9)$$

$$P_{PE} = 2 \frac{a - a_0}{a_0} \left(e_{31} - e_{33} \frac{C_{13}}{C_{33}} \right), \quad (10)$$

$$P_{SP} = (-0.052x - 0.029) (\text{Cm}^{-2}), \quad (11)$$

where x is the Al mole fraction in the AlGaIn layer, a is the lattice constant of the strained layer, a_0 is the length of the hexagonal edge, e_{31} and e_{33} are the piezoelectric coefficients, and C_{13} and C_{33} are the elastic constants. The analytical expressions for the elastic constants and piezoelectric coefficients are given elsewhere.^{41,42} Using Eqs. (9)–(11), the polarization charge of $\sigma_{pol} = \pm 1.23 \times 10^{13}$ cm⁻² has been calculated for the AlGaIn/GaN HEMT simulation.¹⁵ It is worth remembering that the surface donors are placed at $E_C - 1.4$ eV based on the surface donor theory and experimental reports. The electron trap E1 (identified from the DCT experiment) is included in the physical model at $E_C - 0.5$ eV as an acceptor-like state in the GaN buffer region; the electron capture cross section of $\sigma_{nA} = 3 \times 10^{-16}$ cm² is taken from the experimental data, and the hole capture cross section ($\sigma_{nA} = 10^{-20}$ cm²) is assumed.

The Schottky barrier height for the Ni/GaN Schottky contacts is reported as 0.8–0.85 eV.^{43–46} Accordingly, the gate metal work function (Φ_G) is selected as 4.7 eV in the simulation, and the electron affinity (χ) of GaN is 3.9 eV. The Sentaurus device internally computes the Schottky barrier height (Φ_B) according to the well-known expression of $\Phi_B = \Phi_G - \chi$. Figure 5 shows that the transfer (I_{DS} - V_{GS}) characteristics of the AlGaIn/GaN HEMT are simulated at different Φ_G values (from 4.5 to 4.9 eV). A positive shift in threshold

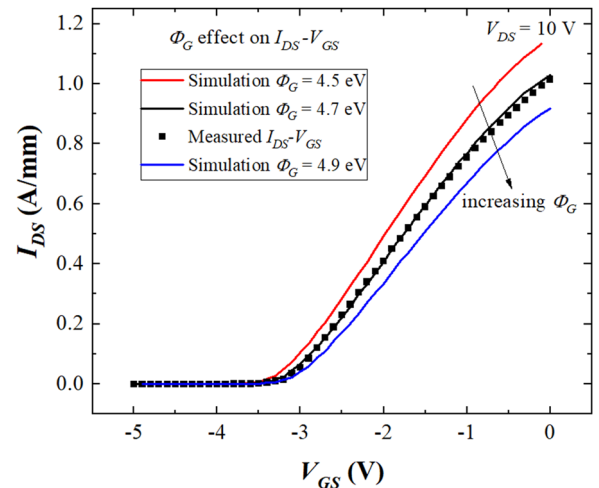


FIG. 5. Simulated transfer (I_{DS} - V_{GS}) characteristics (at $V_{DS} = 10$ V) of the AlGaIn/GaN HEMT for different gate metal work functions ($\Phi_G = 4.5$ – 4.9 eV) at room temperature.

voltage (V_{TH}) is noticed upon increasing Φ_G , as per the following equation:⁴⁷⁻⁴⁹

$$V_{TH} = \Phi_B - \Delta E_C - \frac{qN_d d_d^2}{2\epsilon} - \frac{q\sigma}{\epsilon}(d_d + d_i), \quad (12)$$

where Φ_B is the Schottky barrier height, ΔE_C is the conduction band offset at the AlGaIn/GaN interface, ϵ is the permittivity of the AlGaIn material, N_d is the doping concentration in the AlGaIn barrier layer, d_d is the thickness of the AlGaIn barrier layer, d_i is the thickness of the AlGaIn spacer layer (i.e., total thickness of the AlGaIn layer $d = d_d + d_i$), and σ is the polarization charge at the heterointerface. The magnitude of the threshold voltage $|V_{TH}|$ and drain current (I_{DS}) values are found to decrease with increasing Φ_G (see Fig. 5) due to the corresponding modulation in the 2DEG density under the gate region.

The acceptor trap concentration in the buffer ($N_{TA} = 10^{17} \text{ cm}^{-3}$) is chosen based on the comparison between the measured and simulated DC and transient characteristics. The considered acceptor density (10^{17} cm^{-3}) is found to be more appropriate for the I_{DS} transient simulations (refer to Secs. IV C). The electron mobility and saturation velocity in the GaN are fine tuned to achieve the desired output drain current characteristics in the linear and saturation regions. The important parameters used in the static and transient simulations of the AlGaIn/GaN HEMT are summarized in Table I.

The DC characteristics presented in this article are obtained at room temperature. Figure 6 displays the simulated and measured transfer ($I_{DS}-V_{GS}$) characteristics of the AlGaIn/GaN HEMT at $V_{DS} = 10 \text{ V}$, together with the transconductance (g_m) properties. The TCAD simulation model provides good agreement between the simulated and measured $I_{DS}-V_{GS}$, with the same threshold voltage of $V_{TH} = -3.6 \text{ V}$. It is seen in Fig. 6 that the transconductance initially upsurges with increasing V_{GS} and reaches a maximum value of $\sim 370 \text{ mS/mm}$ around $V_{GS} = -2.5 \text{ V}$. Beyond that voltage, g_m is found to decrease with V_{GS} , thereby resulting in a bell-shaped g_m curve, which has been normally observed in AlGaIn/GaN HEMTs.⁵⁰⁻⁵² The unfavorable decline in the transconductance at higher V_{GS} may be

TABLE I. The important parameters used in the static and transient simulations of AlGaIn/GaN HEMT.

Parameters	Values
Gate work function (Φ_G)	4.7 eV
Polarization charge (σ_{pol})	$\pm 1.23 \times 10^{13} \text{ cm}^{-2}$
Electron affinity (χ) in GaN	3.9 eV
Electron mobility (μ_n) in GaN	$1400 \text{ cm}^2/\text{V s}$
Electron saturation velocity (v_{sat}^n) in GaN	$1.6 \times 10^7 \text{ cm/s}$
Surface donor parameters	$E_{TD} = E_C - 1.4 \text{ eV}$, $N_{TD} = 2 \times 10^{13} \text{ cm}^{-2}$, $\sigma_{nD} = \sigma_{pD} = 10^{-15} \text{ cm}^2$
Buffer trap signatures	$E_{TA} = E_C - 0.5 \text{ eV}$, $N_{TA} = 10^{17} \text{ cm}^{-3}$, $\sigma_{nA} = 3 \times 10^{-16} \text{ cm}^2$, $\sigma_{pA} = 10^{-20} \text{ cm}^2$

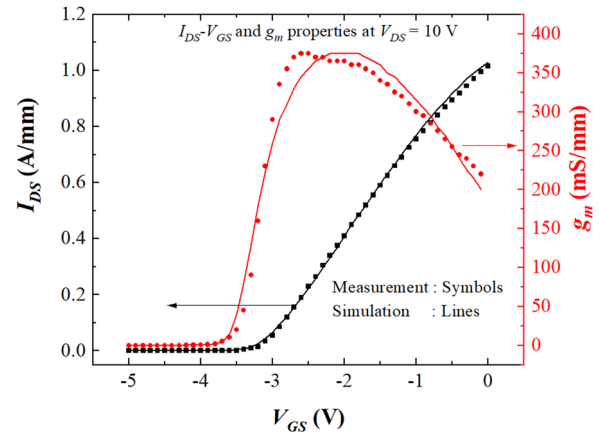


FIG. 6. Comparison of simulated and measured transfer ($I_{DS}-V_{GS}$) characteristics of the AlGaIn/GaN HEMT at $V_{DS} = 10 \text{ V}$ is shown along with the transconductance (g_m) properties at room temperature.

due to the non-linear increase in the source-gate and gate-drain resistances at higher I_{DS} values.⁵⁰⁻⁵² It is also shown in Fig. 6 that the simulated g_m closely tracks the experimental data.

The simulated output ($I_{DS}-V_{DS}$) characteristics of the HEMT are an excellent match with the measured data for different gate voltages ($V_{GS} = -3.5-0 \text{ V}$), as illustrated in Fig. 7. Furthermore, the simulation model has shown its capability in predicting the DC characteristics of other HEMT devices in the same batch/wafer. Hence, the validated DC simulations confirm the reliability of the TCAD physical model.

The detailed studies of the buffer trapping effects on the static $I-V$ characteristics are reported elsewhere;^{17,53} hence, the outcomes are briefly discussed in this article. The simulated energy band diagram under a static bias condition ($V_{DS} = 10 \text{ V}$ and $V_{GS} = -1 \text{ V}$)

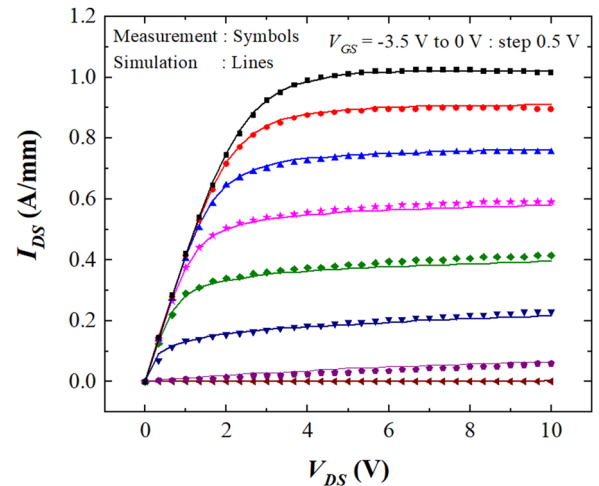


FIG. 7. Simulated output ($I_{DS}-V_{DS}$) characteristics of the AlGaIn/GaN HEMT validated with measured data for varying gate voltages $V_{GS} = -3.5-0 \text{ V}$ at a step of 0.5 V at room temperature.

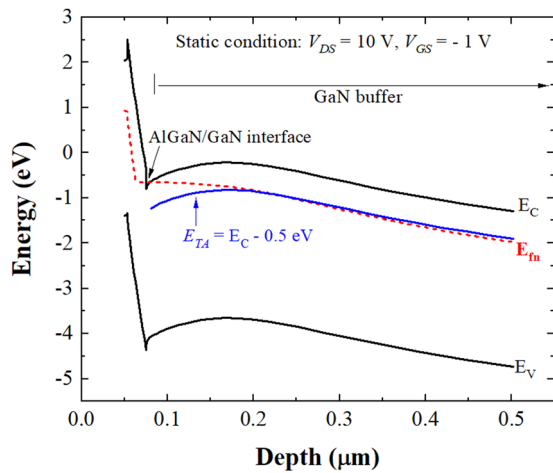


FIG. 8. Simulated energy band diagram under static bias condition ($V_{DS} = 10$ V and $V_{GS} = -1$ V) along the vertical cutline at the gate-edge toward the drain-side.

along the vertical cutline at the gate-edge toward the drain-side is shown in Fig. 8, where E_{fn} and E_{TA} denote the Fermi level and buffer trap energy position, respectively. Note that the buffer traps are taken as acceptor-like states in the simulation. The acceptor traps located below the Fermi level are occupied by electrons and turned into a negatively ionized state (N_{TA}^-). On the other hand, the acceptors positioned above the Fermi level have a neutral state as they are unoccupied. It is identified that almost complete ionization takes place near the 2DEG; then the ionized acceptor density (N_{TA}^-) decreases along the vertical downward direction of the buffer layer due to the relative variation in the Fermi level with respect to E_{TA} , as perceived from Fig. 8. The I_{DS} - V_{DS} properties are simulated by varying the buffer trap concentration N_{TA} (here, $E_{TA} = E_C - 0.5$ eV and $\sigma_{nA} = 3 \times 10^{-16}$ cm² are fixed) and buffer trap energy E_{TA} (with fixed $N_{TA} = 10^{17}$ cm⁻³ and $\sigma_{nA} = 3 \times 10^{-16}$ cm²) and are plotted in Figs. 9(a) and 9(b). As expected, a significant reduction in I_{DS} is noticed after increasing N_{TA} from 8×10^{16} to 1.5×10^{17} cm⁻³ because of the augmented electron trapping in the buffer (N_{TA}^- increases) and the corresponding decline in the 2DEG density. Moreover, I_{DS} reduces when E_{TA} is decreased from $E_C - 0.3$ eV to $E_C - 0.5$ eV [see Fig. 9(b)] due to the relative downward movement of E_{TA} with respect to the Fermi level^{17,53} (refer to Fig. 8). The magnitude of threshold voltage $|V_{TH}|$ is also found to decrease with increasing N_{TA} and for deeper E_{TA} values, as noted from the simulated transfer characteristics (not shown). It is observed that the electron and hole capture cross sections (σ_{nA} and σ_{pA}) of the buffer trap do not change the DC properties. Overall, the simulation results reveal that electron trapping in the buffer layer reduces the static I_{DS} of the AlGaIn/GaN HEMT.

C. Simulated DCT spectroscopy

Similar to the experimental observations, the simulated DCT signal amplitude is not affected by the duration of the filling pulse ($t_f = 10$ μ s to 100 ms). For better visualization of the DCT peak variations while changing the buffer trap parameters (E_{TA} , N_{TA} , and σ_{nA}), the DCT properties attained with $t_f = 100$ μ s (showing a distinct

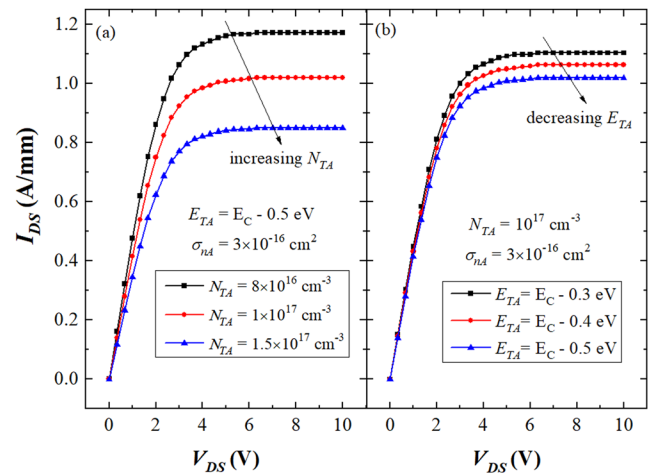


FIG. 9. Simulated I_{DS} - V_{DS} properties of the AlGaIn/GaN HEMT by varying (a) buffer trap concentration $N_{TA} = 8 \times 10^{16}$ to 1.5×10^{17} cm⁻³ (with fixed $E_{TA} = E_C - 0.5$ eV and $\sigma_{nA} = 3 \times 10^{-16}$ cm²) and (b) buffer trap energy $E_{TA} = E_C - 0.3$ eV to $E_C - 0.5$ eV (fixed $N_{TA} = 10^{17}$ cm⁻³ and $\sigma_{nA} = 3 \times 10^{-16}$ cm²).

peak) are presented in this section. The measured DCT at $t_f = 100$ μ s reveals a single trap E1 at $E_C - 0.5$ eV (refer to Fig. 4). Hence, the I_{DS} transients are simulated by incorporating the buffer trap E1 signatures used in the DC simulations. Figures 10(a) and 10(b) depict the simulated and experimental DCT spectra acquired with filling times of 10 and 100 μ s for the AlGaIn/GaN HEMT; the solid lines and dots represent the simulated and experimental DCT, respectively. The DCT response is simulated with the trap-filling biasing condition of pulsed V_{DS} from 10 to 20 V and the subsequent detrapping bias at $V_{DS} = 10$ V and $I_{DS} = \sim 50$ mA/mm. It is shown that the simulated DCT properties closely track the measured spectra for both the filling times ($t_f = 10$ and 100 μ s) over the temperature range of 25–100 °C. Similar agreement is observed in the DCT acquired for other filling times of 1 ms. Arrhenius analysis of the simulated DCT also yields the same activation energy (~ 0.5 eV) and electron capture cross section ($\sim 3 \times 10^{-16}$ cm²), as considered in the simulation. Furthermore, a good matching is attained between the simulated and experimental DCT for different V_{DS} pulsing conditions: (1) The initial V_{DS} filling pulse is switched from 10 to 15 V, and the subsequent detrapping transient is recorded at $V_{DS} = 10$ V. (2) The initial V_{DS} filling pulse is raised from 5 to 20 V, and the detrapping transient is acquired at $V_{DS} = 5$ V. Therefore, the DCT simulations are validated for the different trap-filling times and also for different V_{DS} pulsing conditions.

The DCT simulation investigations are extended for the following cases: (1) specifying the buffer traps as donor-like states and (2) excluding the buffer traps from the physical model. However, the flat I_{DS} transient response is obtained in both these cases, i.e., no I_{DS} transient recovery process (maximum I_{DS} value reached) in the DCT spectra due to the absence of electron trapping in the buffer. It is reiterated that the TCAD model incorporating the acceptor-type trap at $E_C - 0.5$ eV in the GaN buffer quantitatively reproduces the measured DCT spectra. Therefore, the DCT simulation results confirm the existence of acceptor-type electron trap E1 at $E_C - 0.5$ eV in the GaN buffer layer. The deep-level traps in the Fe-doped buffer

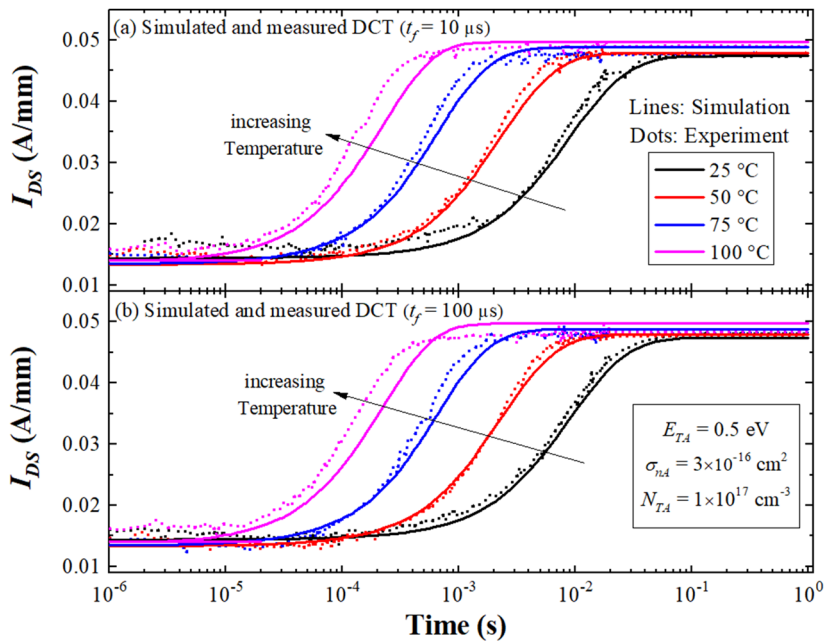


FIG. 10. Simulated DCT characteristics at the two different filling times (t_f) of (a) 10 μs and (b) 100 μs for the AlGaIn/GaN HEMT (Fe-doped buffer) compared with the measured spectra over the temperature range of 25–100 $^{\circ}\text{C}$ with trap-filling biasing condition of pulsed V_{DS} from 10 to 20 V and the subsequent detrapping bias at $V_{DS} = 10$ V and $I_{DS} = \sim 50$ mA/mm.

layer have been detected with the apparent energy between $E_C - 0.4$ and $E_C - 0.7$ eV.^{1–5,10,12,13,15–20,54} It is reported^{4,5} that the electrically active traps at $E_C - (0.5–0.7)$ eV can be physically present in the buffer region even without Fe-doping and most likely originate from the intrinsic point defects of GaN, but their concentration increases with the amount of Fe-doping in the buffer. Based on the DCT simulation results and reported works in the literature, the electron trap E1 is attributed to the intrinsic point defect of GaN linked to the Fe-doping in the buffer. Several authors^{2–4,10} identified the deep electron trap at $E_C - 0.6$ eV in the Fe-doped buffer layers. Meneghini *et al.*² demonstrated that the buffer trap at $E_C - 0.6$ eV is responsible for the current collapse in the AlGaIn/GaN HEMT. Accordingly, another electron trap E2 at $E_C - 0.6$ eV is also ascribed to the Fe-doping dependent intrinsic point defect.

Figure 11(a) shows the simulated DCT spectra by varying the buffer trap energy (E_{TA}) from $E_C - 0.3$ eV to $E_C - 0.5$ eV at 25 $^{\circ}\text{C}$, where $N_{TA} = 10^{17}$ cm^{-3} and $\sigma_{nA} = 3 \times 10^{-16}$ cm^2 are fixed in this case. The corresponding DCT derivative spectra for different E_{TA} are plotted in Fig. 11(b). The DCT peak shifts toward longer time constants (τ_n) for the deeper trap energies, according to the emission rate equation (6). At the beginning of the transient (t_{0+}), a notable drop in I_{DS} is seen in Fig. 11(a) with decreasing E_{TA} from $E_C - 0.3$ eV to $E_C - 0.5$ eV. Afterward, the I_{DS} transient recovery process starts, as shown in Fig. 11(a), due to the electron detrapping mechanism. After the transient recovery, I_{DS} reaches the steady-state value at the end of the transient (t_{∞}); some of the buffer traps (located near the 2DEG) are still always occupied by electrons even under static conditions,^{17,53} as perceived from Fig. 8. For this reason, a considerable reduction in $I_{DS}(t_{\infty})$ is noted for deeper E_{TA} , analogous to the static $I-V$ properties in Fig. 9(b). Hence, the energy position of the buffer trap affects both τ_n and static I_{DS} .

The simulated DCT and the respective derivative spectra by varying the electron capture cross section (σ_{nA}) of the buffer trap

at $E_C - 0.5$ eV ($N_{TA} = 10^{17}$ cm^{-3}) are depicted in Figs. 12(a) and 12(b). The DCT peak moves to lower τ_n upon increasing σ_{nA} from 5×10^{-17} to 5×10^{-15} cm^2 . Equation (5) dictates that the electron capture rate is directly proportional to the electron capture cross section. As a result, $I_{DS}(t_{0+})$ decreases with increasing σ_{nA} at the beginning of the transient, as shown in Fig. 12(a). Furthermore, variations in the DCT amplitude (ΔI) and $\partial I_{DS}/\partial \log_{10}(t)$ are found to be larger for higher σ_{nA} . Nevertheless, the same steady-state $I_{DS}(t_{\infty})$ is reached for all σ_{nA} values, and this observation is consistent with

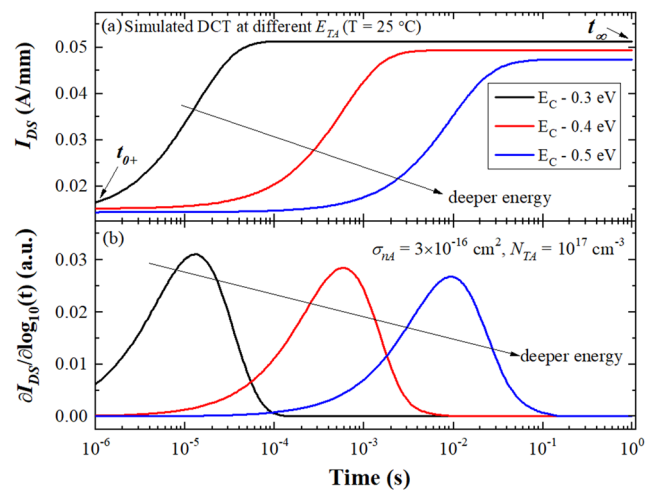


FIG. 11. (a) Simulated DCT spectra for the HEMT ($T = 25$ $^{\circ}\text{C}$) by decreasing the buffer trap energy $E_{TA} = E_C - 0.3$ eV to $E_C - 0.5$ eV ($N_{TA} = 10^{17}$ cm^{-3} and $\sigma_{nA} = 3 \times 10^{-16}$ cm^2 are fixed). (b) The corresponding DCT derivative spectra at different E_{TA} .

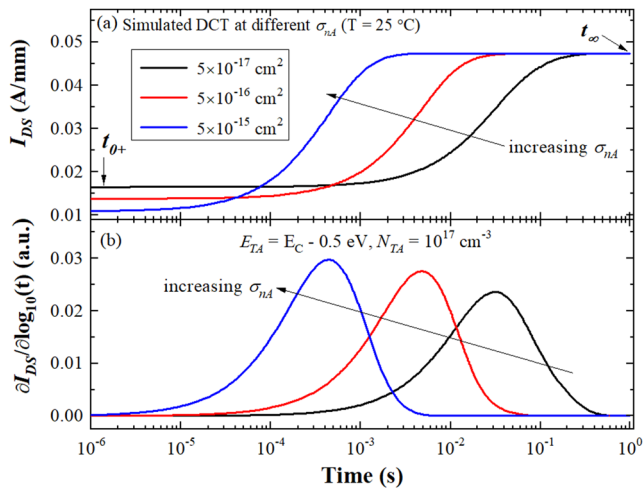


FIG. 12. (a) Simulated DCT characteristics by changing the electron capture cross section ($\sigma_{nA} = 5 \times 10^{-17}$ – 5×10^{-15} cm^2) of the buffer trap at $E_C - 0.5$ eV ($N_{TA} = 10^{17}$ cm^{-3}). (b) The respective DCT derivative spectra for various σ_{nA} values.

the fact that static I - V properties are not affected by σ_{nA} . However, the DCT characteristics remain unchanged by the hole capture cross section (σ_{pA}) of the buffer trap.

The simulated DCT spectra for different concentrations (N_{TA}) of the buffer trap at $E_C - 0.5$ eV ($\sigma_{nA} = 3 \times 10^{-16}$ cm^2) are plotted in Fig. 13(a). No considerable change in τ_n is noted for increasing N_{TA} . In fact, N_{TA} reduces the overall static I_{DS} value of the DCT signal, as correlated with the DC characteristics in Fig. 9(a). By looking at Fig. 13(a), it appears that the magnitude of the DCT signal (ΔI) is not altered by N_{TA} . Moreover, a slight decline in ionized trap density (N_{TA}^-) is anticipated with the increase in temperature because of the augmented emission rate.⁵⁵ Conversely, nonlinear

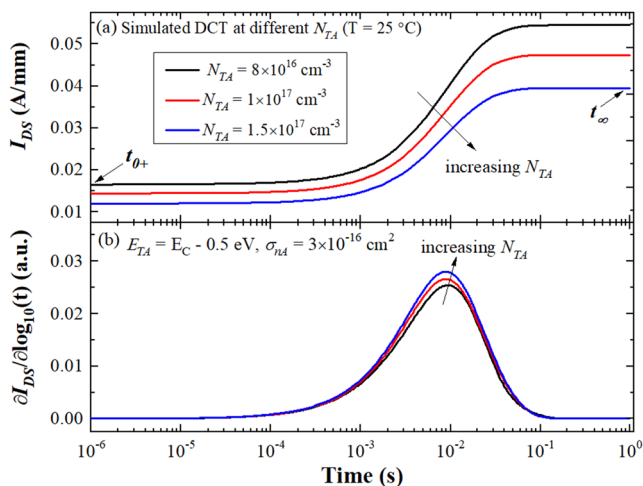


FIG. 13. (a) Simulated DCT properties for increasing trap concentrations ($N_{TA} = 8 \times 10^{16}$ to 1.5×10^{17} cm^{-3}) of the buffer trap at $E_C - 0.5$ eV ($\sigma_{nA} = 3 \times 10^{-16}$ cm^2). (b) The corresponding derivative spectra at different N_{TA} .

$\partial I_{DS}/\partial \log_{10}(t)$ variation has been observed with increasing temperature from the measured DCT spectroscopy in Fig. 2(b), suggesting that ΔI may not be linked with the trap concentration. It is visualized that the buffer traps take nearly the same amount of time (identical detrapping times^{17,33}) to reach the steady-state I_{DS} even after modifying N_{TA} from 8×10^{16} to 1.5×10^{17} cm^{-3} . However, a small increase in the DCT derivative signal $\partial I_{DS}/\partial \log_{10}(t)$ is realized in Fig. 13(b) with increasing N_{TA} , which is contrary to our hypothesis on ΔI . Therefore, further studies are underway to understand the DCT signal amplitude dependency on the buffer trap concentration. From the simulation results, it is concluded that the carrier emission time constant strongly depends on the energy level and electron capture cross section of the buffer trap, i.e., emission time constant increases (emission rate reduces) with decreasing electron capture cross sections and for deeper trap energies. This observation is helpful in modeling a slow detrapping mechanism in the AlGaIn/GaN HEMT simulations. On the other hand, the emission time constant does not change with the acceptor concentration.

V. CONCLUSION

The DCT characterization and TCAD simulation studies are carried out to investigate electron trapping in the AlGaIn/GaN HEMT with Fe-doped buffer. Two deep-level traps E1 at $E_C - 0.5$ eV and E2 at $E_C - 0.6$ eV are identified in the HEMT from the DCT experiments. The DCT signal amplitude of E1 and E2 is not affected by the duration of the trap-filling pulse, suggesting that traps E1 and E2 are associated with the Fe-doping dependent point defects of GaN. From the simulated DC properties, it is found that electron trapping in the buffer reduces the static I_{DS} value of the AlGaIn/GaN HEMT. The simulated DCT spectra are validated with the measured data in the temperature range of 25–100 °C. The DCT simulations confirm the presence of acceptor-type electron traps (E1 and E2) in the GaN buffer layer. Furthermore, the carrier emission time constant is found to increase (emission rate reduces) with decreasing electron capture cross sections and for deeper trap energies, while the same τ_n is not controlled by the buffer trap concentration.

ACKNOWLEDGMENTS

We greatly appreciate and acknowledge the Agence Nationale de la Recherche (ANR) and the Direction Générale de l'Armement (DGA), France, for funding, under Contract No. ANR-17-ASTR-0007-01 (COMPACT project).

AUTHOR DECLARATIONS

Conflict of Interest

The authors have no conflicts to disclose.

Author Contributions

All authors contributed equally to this work.

DATA AVAILABILITY

The data that support the findings of this study are available from the corresponding author upon reasonable request. The data

are not publicly available due to the intellectual property protection rights.

REFERENCES

- ¹M. Silvestri, M. J. Uren, and M. Kuball, *Appl. Phys. Lett.* **102**, 073501 (2013).
- ²M. Meneghini, I. Rossetto, D. Bisi, A. Stocco, A. Chini, A. Pantellini, C. Lanzieri, A. Nanni, G. Meneghesso, and E. Zanoni, *IEEE Trans. Electron Devices* **61**, 4070 (2014).
- ³O. Axelsson, S. Gustafsson, H. Hjelmgren, N. Rorsman, H. Blanck, J. Spletstoeser, J. Thorpe, T. Roedle, and M. Thorsell, *IEEE Trans. Electron Devices* **63**, 326 (2015).
- ⁴J. Bergsten, M. Thorsell, D. Adolph, J.-T. Chen, O. Kordina, E. O. Sveinbjornsson, and N. Rorsman, *IEEE Trans. Electron Devices* **65**, 2446 (2018).
- ⁵I. Rossetto, D. Bisi, C. de Santi, A. Stocco, G. Meneghesso, E. Zanoni, and M. Meneghini, "Performance-limiting traps in GaN-based HEMTs: From native defects to common impurities," in *Power GaN Devices Materials, Applications and Reliability* (Springer, Switzerland, 2017), p. 197.
- ⁶J. Joh and J. A. del Alamo, *IEEE Trans. Electron Devices* **58**, 132 (2011).
- ⁷D. Bisi, M. Meneghini, C. de Santi, A. Chini, M. Dammann, P. Bruckner, M. Mikulla, G. Meneghesso, and E. Zanoni, *IEEE Trans. Electron Devices* **60**, 3166 (2013).
- ⁸G. Meneghesso, M. Meneghini, D. Bisi, I. Rossetto, A. Cester, U. K. Mishra, and E. Zanoni, *Semicond. Sci. Technol.* **28**, 074021 (2013).
- ⁹M. Meneghini, G. Meneghesso, and E. Zanoni, "Trapping and degradation mechanisms in GaN-based HEMTs," in *Gallium Nitride (GaN) Physics, Devices, and Technology* (CRC Press, Boca Raton, 2016), p. 327.
- ¹⁰A. Benvegnù, D. Bisi, S. Laurent, M. Meneghini, G. Meneghesso, D. Barataud, E. Zanoni, and R. Quere, *Int. J. Microwave Wireless Technol.* **8**, 663 (2016).
- ¹¹X. Zheng, S. Feng, Y. Zhang, and J. Yang, *Microelectron. Reliab.* **63**, 46 (2016).
- ¹²M. Bouslama, V. Gillet, C. Chang, J.-C. Nallatamby, R. Sommet, M. Prigent, R. Quere, and B. Lambert, *IEEE Trans. Microwave Theory Technol.* **67**, 2475 (2019).
- ¹³P. V. Raja, M. Bouslama, S. Sarkar, K. R. Pandurang, J.-C. Nallatamby, N. DasGupta, and A. DasGupta, *IEEE Trans. Electron Devices* **67**, 2304 (2020).
- ¹⁴C. Potier, J.-C. Jacquet, C. Dua, A. Martin, M. Campovecchio, M. Oualli, O. Jardel, S. Piotrowicz, S. Laurent, R. Aubry, O. Patard, P. Gamarra, M.-A. di Forte-Poisson, S. L. Delage, and R. Quéré, *Int. J. Microwave Wireless Technol.* **7**, 287 (2015).
- ¹⁵N. K. Subramani, J. Couvidat, A. A. Hajjar, J.-C. Nallatamby, R. Sommet, and R. Quere, *IEEE J. Electron Devices Soc.* **5**, 175 (2017).
- ¹⁶M. Bouslama, R. Sommet, and J.-C. Nallatamby, in *14th European Microwave Integrated Circuits Conference (EuMIC), Paris, France* (IEEE, 2019), pp. 29–32.
- ¹⁷P. V. Raja, J.-C. Nallatamby, N. DasGupta, and A. DasGupta, *Solid-State Electron.* **176**, 107929 (2021).
- ¹⁸N. K. Subramani, J. Couvidat, A. A. Hajjar, J.-C. Nallatamby, D. Floriot, M. Prigent, and R. Quere, *IEEE Electron Device Lett.* **38**, 1109 (2017).
- ¹⁹N. K. Subramani, J. Couvidat, A. A. Hajjar, J.-C. Nallatamby, and R. Quere, *IEEE Electron Device Lett.* **39**, 107 (2018).
- ²⁰M. Bouslama, A. A. Hajjar, S. Laurent, N. K. Subramani, J.-C. Nallatamby, and M. Prigent, in *International Workshop on Integrated Nonlinear Microwave and Millimetre-wave Circuits (INMMIC), Brive La Gaillarde, France* (IEEE, 2018), pp. 1–3.
- ²¹G. Meneghesso, G. Verzellesi, R. Pierobon, F. Rampazzo, A. Chini, U. K. Mishra, C. Canali, and E. Zanoni, *IEEE Trans. Electron Devices* **51**, 1554 (2004).
- ²²J. M. Tirado, J. L. Sanchez-Rojas, and J. I. Izpura, *Semicond. Sci. Technol.* **21**, 1150 (2006).
- ²³J. M. Tirado, J. L. Sanchez-Rojas, and J. I. Izpura, *IEEE Trans. Electron Devices* **54**, 410 (2007).
- ²⁴W. D. Hu, X. S. Chen, F. Yin, J. B. Zhang, and W. Lu, *J. Appl. Phys.* **105**, 084502 (2009).
- ²⁵A. Chini, F. Soci, M. Meneghini, G. Meneghesso, and E. Zanoni, *IEEE Trans. Electron Devices* **60**, 3176 (2013).
- ²⁶W. Zhang, Y. Zhang, W. Mao, X. Ma, J. Zhang, and Y. Hao, *IEEE Electron Device Lett.* **34**, 45 (2013).
- ²⁷C. Miccoli, V. C. Martino, S. Reina, and S. Rinaudo, *IEEE Electron Device Lett.* **34**, 1121 (2013).
- ²⁸Y. Zhang, S. Feng, H. Zhu, C. Guo, B. Deng, and G. Zhang, *IEEE Electron Device Lett.* **35**, 345 (2014).
- ²⁹M. J. Anand, G. I. Ng, S. Arulkumaran, B. Syamal, and X. Zhou, *Appl. Phys. Express* **8**, 104101 (2015).
- ³⁰S. Mukherjee, E. E. Patrick, and M. E. Law, *ECS J. Solid State Sci. Technol.* **6**, S3093 (2017).
- ³¹A. Chini, G. Meneghesso, M. Meneghini, F. Fantini, G. Verzellesi, A. Patti, and F. Iucolano, *IEEE Trans. Electron Devices* **63**, 3473 (2016).
- ³²Sentaurus TCAD User Guide, Version N-2017.09, Synopsys Inc., San Jose, CA, USA, 2017.
- ³³X. Zhou, Z. Feng, L. Wang, Y. Wang, Y. Lv, S. Dun, and S. Cai, *Solid-State Electron.* **100**, 15 (2014).
- ³⁴M. Molnár, D. Donoval, J. Kuzmík, J. Marek, A. Chvála, P. Příbytný, M. Mikolášek, K. Rendek, and V. Palankovski, *Appl. Surf. Sci.* **312**, 157 (2014).
- ³⁵D. B. Christian, Ph.D. thesis, University of Padova, Italy, 2010.
- ³⁶G. Longobardi, F. Udrea, S. Sque, G. A. M. Hurkx, J. Croon, E. Napoli, and J. Šonký, *IEEE Electron Device Lett.* **35**, 27 (2013).
- ³⁷N. K. Subramani, A. K. Sahoo, J.-C. Nallatamby, R. Sommet, N. Rolland, F. Medjdoub, and R. Quere, *IEEE Trans. Microwave Theory Tech.* **64**, 1351 (2016).
- ³⁸I. P. Smorchkova, C. R. Elsass, J. P. Ibbetson, R. Veturly, B. Heying, P. Fini, E. Haus, S. P. DenBaars, J. S. Speck, and U. K. Mishra, *J. Appl. Phys.* **86**, 4520 (1999).
- ³⁹J. P. Ibbetson, P. T. Fini, K. D. Ness, S. P. DenBaars, J. S. Speck, and U. K. Mishra, *Appl. Phys. Lett.* **77**, 250 (2000).
- ⁴⁰H. K. Cho, C. S. Kim, and C.-H. Hong, *J. Appl. Phys.* **94**, 1485 (2003).
- ⁴¹O. Ambacher, B. Foutz, J. Smart, J. R. Shealy, N. G. Weimann, K. Chu, M. Murphy, A. J. Sierakowski, W. J. Schaff, L. F. Eastman, R. Dimitrov, A. Mitchell, and M. Stutzmann, *J. Appl. Phys.* **87**, 334 (2000).
- ⁴²R. Quay, "III-N materials, and the state-of-the-art of devices and circuits," in *Gallium Nitride Electronics* (Springer, Germany, 2008), p. 2.
- ⁴³N. Miura, T. Nanjo, M. Suita, T. Oishi, Y. Abe, T. Ozeki, H. Ishikawa, T. Egawa, and T. Jimbo, *Solid-State Electron.* **48**, 689 (2004).
- ⁴⁴M. L. Lee, J. K. Sheu, and S. W. Lin, *Appl. Phys. Lett.* **88**, 032103 (2006).
- ⁴⁵O. Lazăr, J.-G. Tartarin, B. Lambert, C. Moreau, J. L. Roux, and J. L. Muraro, in *IEEE MTT-S International Microwave Symposium, Phoenix, AZ, USA* (IEEE, 2015), pp. 1–4.
- ⁴⁶W. Lim, J.-H. Jeong, J.-H. Lee, S.-B. Hur, J.-K. Ryu, K.-S. Kim, T.-H. Kim, S. Y. Song, J.-I. Yang, and S. J. Pearton, *Appl. Phys. Lett.* **97**, 242103 (2010).
- ⁴⁷M. Li and Y. Wang, *IEEE Trans. Electron Devices* **55**, 261 (2007).
- ⁴⁸W. E. Muhea, F. M. Yigletu, R. Cabre-Rodon, and B. Iniguez, *IEEE Trans. Electron Devices* **65**, 901 (2018).
- ⁴⁹N. Karumuri, S. Turuvekere, N. DasGupta, and A. DasGupta, *IEEE Trans. Electron Devices* **61**, 2343 (2014).
- ⁵⁰C.-H. Chen, R. Sadler, D. Wang, D. Hou, Y. Yang, W. Yau, W. Sutton, J. Shim, S. Wang, and A. Duong, *Solid-State Electron.* **126**, 115 (2016).
- ⁵¹Y.-R. Wu, M. Singh, and J. Singh, *IEEE Trans. Electron Devices* **52**, 1048 (2005).
- ⁵²S. Vitanov, V. Palankovski, S. Maroldt, and R. Quay, in *Proceedings of European Solid-State Device Research Conference: Fringe Poster Session, Sevilla, Spain, 2010*.
- ⁵³P. V. Raja, N. DasGupta, and A. DasGupta, in *4th IEEE International Conference on Emerging Electronics (ICEE), Bangalore, India* (IEEE, 2018), pp. 1–6.
- ⁵⁴D. W. Cardwell, A. Sasikumar, A. R. Arehart, S. W. Kaun, J. Lu, S. Keller, J. S. Speck, U. K. Mishra, S. A. Ringel, and J. P. Pelz, *Appl. Phys. Lett.* **102**, 193509 (2013).
- ⁵⁵P. Blood and J. W. Orton, *The Electrical Characterization of Semiconductors: Majority Carriers and Electron States* (Academic Press, London, 1992).